INSIGHTS ON THE SOURCE CHARACTERISTICS OF THE 2016–2017 CENTRAL ITALY EARTHQUAKE SEQUENCE

H. W. Wang(1), Y. F. Ren(2), R. Z. Wen(3)

(1) *Harbin, P. R. China, Institute of Engineering Mechanics, China Earthquake Administration, whw1990413@163.com*
(2) *Harbin, P. R. China, Institute of Engineering Mechanics, China Earthquake Administration, renyefei@iem.ac.cn*
(3) *Harbin, P. R. China, Institute of Engineering Mechanics, China Earthquake Administration, ruizhi@iem.ac.cn*

Abstract

The 2016–2017 central Italy earthquake sequence was initiated by an M_L 6.0 mainshock on 24 August 2016 at 01:36:32 (UTC) close to the town of Accumoli. About two months later, another two destructive earthquakes (M_L 5.9 on 26 October at 19:18:06 (UTC) and M_L 6.1 on 30 October at 06:40:18 (UTC)) subsequently shocked the area to the NNW of the M_L 6.0 event. Up until 24 August 2017, this sequence comprised ~1100 events of $M_L \geq 3.0$. With respect to this sequence, the Engineering Strong-Motion database was formally released. It comprised about 8000 high-quality, manually processed strong-motion recordings collected at 337 stations in 106 shallow crustal events of M_L = 3.1–6.1. To the end of analyzing the source characteristics of the 2016–2017 central Italy earthquake sequence, source spectra from 78 earthquakes of M_L = 3.5–6.1 were separated from the S-wave Fourier spectra of the selected 5135 strong-motion recordings using the two-step nonparametric generalized inversion technique. Source parameters (e.g., corner frequency, stress drop) were estimated from the source spectra, which math well with the well-known ω-square model. Stress drops were found mainly in the range 0.113–12.190 MPa. The significant dependence of stress drop on magnitude indicates the breakdown of earthquake self-similar scaling in this sequence. The low stress drops for small events following the release of high stress by the mainshock might have led to stress accumulation on the unruptured fault, which could explain the subsequent occurrence of multiple major events. Furthermore, the source rupture directivity for 36 out of the 78 events were investigated based on the azimuthal variation of apparent source spectra. Significant azimuthal variation was observed at specific frequency bands (generally, over corner frequencies) for 10 events with strong rupture directivity, which was verified by the stable estimation of rupture plane. Their rupture parameters all confirmed the unilateral ruptures predominantly on the NNW–SSE-striking fault with fast rupture velocity, i.e., 2.52–2.84 km/s. Rupture parameters for an additional four events with stable estimated rupture plane, including the M_L6.0 mainshock, were also analyzed in this study. The four events were characterized by slow rupture velocity causing weak directivity effects. According to the rupture parameters for the 14 events, prevailing SSE or SEE (NNW or NNE) rupture directivity was a common feature for events to the north (south) of the mainshock in this earthquake sequence.

Keywords: central Italy earthquake, source spectra, stress drop, earthquake self-similar scaling, rupture directivity

1. Introduction

On 24 August 2016 at 01:36:32 (UTC), an M_L 6.0 earthquake close to the town of Accumoli initiated the 2016–2017 central Italy seismic sequence. Another two destructive earthquakes, M_L 5.9 on 26 October at 19:18:06 (UTC) and M_L 6.1 on 30 October at 06:40:18 (UTC), subsequently shocked the area to the NNW of the M_L 6.0 event about two months later. The largest magnitude M_L 6.1 event in this sequence occurred between the epicenters of the M_L 6.0 and M_L 5.9 events. A further four $M_L > 5.0$ events struck the southernmost portion of this sequence on 18 January 2017. Up until 24 August 2017, this sequence comprised ~1100 events of $M_L \geq 3.0$ (http://cnt.rm.ingv.it), primarily nucleated at a depth of about 7–12 km. This sequence activated ~80-km-long NNW–SSE-trending normal fault systems that included the Mt. Vettore–Mt. Bove fault system and the Laga Mts. fault system, which generally strike ~N155° and dipping ~50° toward the southwest [1, 2, 3]. Strong interaction between the pre-existing compressional thrusts and the younger and active normal faults explains the seismicity pattern of this sequence [1, 2].

Central Italy, one of the most seismically active regions in Italy, has suffered frequently moderate events, e.g., the 2009 M_w 6.1 L'Aquila earthquake and the 1997 M_w 6.0 Colfiorito earthquake. The 2016–2017 central Italy seismic sequence filled exactly the spatial seismic gap between the ruptures of the 2009 L'Aquila sequence and the 1997 Umbria–Marche sequence (shown in Fig. 1). The study of source characteristics represents an important basis for interpretation of seismic damage and earthquake physics. Immediately after the M_L 6.0 mainshock, studies were performed to investigate the source characteristics of this sequence. The kinematic source models for the M_L 6.0 mainshock and two subsequent major earthquakes (M_L 5.9 and 6.1) were inverted to reveal the slip heterogeneity, rupture directivity, and seismogenic mechanism [1, 2, 3, 4]. The horizontal source rupture directivity for the M_L 6.0 mainshock and strong aftershocks were also investigated [5, 6].

The source characteristics (i.e., earthquake self-similar scaling and source rupture directivity) of the 1997 Umbria–Marche and 2009 L'Aquila seismic sequences in central Italy have been investigated in many studies that have considered the estimation of earthquake hazard [7, 8, 9, 10, 11, 12]. In this study, we attempted to investigate the source characteristics of the 2016–2017 central Italy seismic sequence based on source spectra separated from the S-wave Fourier amplitude spectra using a nonparametric generalized inversion technique (GIT). The earthquake self-similar scaling in this sequence was evaluated from the dependence of the stress drop on moment magnitude, and the source rupture directivity was discussed according to the variations of the apparent source spectra versus the station azimuths.

2. Dataset and methodology

The Engineering Strong-Motion database (http://esm.mi.ingv.it) was formally released for this seismic sequence. It comprised about 8000 high-quality, manually processed strong-motion recordings with hypocentral distances (R) within the range 6.2–429.5 km, collected at 337 stations in 106 shallow crustal events of M_L = 3.1–6.1. The data processes performed in producing the Engineering Strong-Motion database mainly consisted of baseline correction and Butterworth band-pass filtering. Generally, the low-cut corner frequencies (f_L) were found < 0.2 Hz and the high-cut corner frequencies were found equal to 30 Hz for most recordings.

For the purposes of spectral inversion analysis, we selected 5135 ground-motion recordings obtained at 142 surface stations during 78 events of M_L = 3.5–6.1 (as shown in Fig. 1) based on the following criteria: 1) maximal horizontal PGA < 100 cm/s^2; 2) hypocentral distance $R \leq 100$ km; and 3) given criteria 1) and 2), each selected event had to be recorded by at least 10 of the considered stations, each of which recorded at least 10 of the selected events. We extracted and cosine-tapered the S waves of the horizontal components of the selected recordings and we computed and smoothed the S-wave Fourier amplitude spectra at 300 frequencies uniformly spaced on the logarithmic scale from 0.25–30 Hz. The root mean square average of the Fourier amplitude spectra at two horizontal components was used to represent the horizontal ground motion in the frequency domain. Criteria of an SNR threshold of 5.0 and usable frequency no smaller than $1.25f_L$ [13] were adopted simultaneously to select the usable portion of the Fourier spectra. The frequency band of 0.25–20 Hz was finally applied in this study to guarantee data redundancy in the spectral inversion.

We used the two-step nonparametric GIT [8] to separate simultaneously the source spectra, site response functions, and propagation path attenuation from the observed ground motions in the frequency domain. The nonparametric path attenuation, which was constrained as a smooth function of distance with a value of 1 at the reference distance R_0 = 6.2 km, was first determined and further used to corrected the S-wave spectral amplitudes in the second step for estimating the source spectra and site response functions. The rock station LSS (class-A site, V_{S30} = 1091 m/s) was selected as the reference site to remove the trade-offs between source and site effects in the second step. The H/V spectral ratios of the 73 strong-motion data recorded at the LSS station during 2009–2017, with maximum PGA of ~50 cm/s^2, were calculated, and the average spectral ratio was used as the site response.

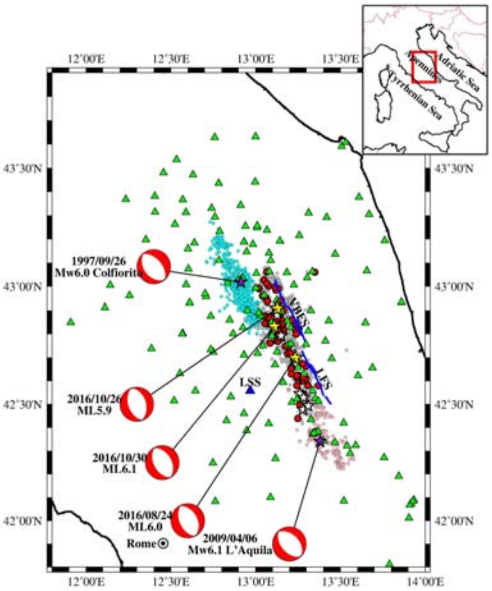

Fig. 1 – Locations of epicenters of earthquakes (red dots and yellow and white stars) and strong-motion stations (triangles) used in this study. Gray, cyan, and pink dots represent events in the 2016–2017 central Italy 1997 Umbria–Marche and 2009 L'Aquila seismic sequences, respectively. Yellow stars represent three major earthquakes (M_L = 6.0, 5.9, and 6.1) and white stars represent six events of M_L > 5.0. Purple stars represent the 2009 M_w 6.1 L'Aquila and 1997 M_w 6.0 Colfiorito earthquakes.

3. Earthquake self-similar scaling

The inverted source acceleration spectra for the considered events are shown in Fig. 2(a). The bootstrap analysis was first performed to assess the stability of the inverted source spectra. Fig. 2(b) shows the source spectra from 100 bootstrap inversions for six typical events, compared with the inverted source spectra using the whole data set. It was found that the deviation of source spectra in bootstrap inversions from the source spectra obtained using the whole data set remains small, implying that the source spectra are stable.

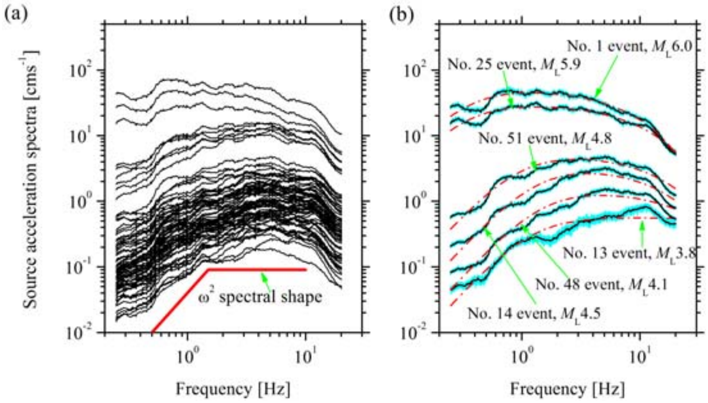

Fig. 2 – (a) Inverted source acceleration spectra for events considered in this study. (b) Best-fitting theoretical spectra to the inverted spectra for six typical events.

The spectral shapes generally match well the well-known ω-square source model [14], except at high frequencies (> ~10 Hz). However, it is striking that rapid decay universally appears in the high-frequency spectra. This could be ascribed to the high-frequency κ decay, usually expressed in the form exp(-πfκ). The high-frequency κ decay that really exists at the reference site but not considered might move into the source spectra, as has been observed by some other studies, e.g., [15]. Thus, our study considered high-frequency κ decay in the inverted source spectrum. The inverted source spectrum can be expressed theoretically as

$$S(f) = (2\pi f)^2 \frac{R_{\Theta\Phi} VF}{4\pi\rho\beta^3 R_0} \frac{M_0}{1+(f/f_c)^2} \exp(-\pi f\kappa) \quad , \tag{1}$$

where M_0 and f_c are the seismic moment and corner frequency, respectively. Here, $R_{\Theta\Phi}$ is set to 0.55 to account for the average radiation pattern over a suitable range of azimuths and take-off angles [16], $V = 1/\sqrt{2}$ represents the partitioning of the total S-wave energy into horizontal components, $F = 2$ is the free surface factor, ρ is the density in the vicinity of the source (set to 2.6 g/cm3 according to the central Italian Apennines model in [17]). We applied a grid-searching technique to retrieve M_0, f_c, and κ for individual events. The reliability of the grid-searching technique for estimating the source parameters were also systematically evaluated. As shown in Fig. 2(b) for six typical events, the theoretical and inverted spectra are mostly in good agreement.

Earthquake self-similar scaling is a controversial issue characterized by a constant stress drop ($\Delta\sigma$) over a wide range of earthquake sizes. It was originally recognized by [18] and it has been observed in large numbers of earthquakes, e.g., global moderate–large earthquakes [19]. However, the breakdown of earthquake self-similar scaling has been verified in certain specific seismic sequences, e.g., the 2009 L'Aquila seismic sequence [12]. Whether self-similar scaling was followed by the 2016–2017 central Italy seismic sequence was investigated in this study. Following [14], the stress drop can be expressed as:

$$\Delta\sigma = \frac{7M_0}{16}\left(\frac{2\pi f_c}{2.34\beta}\right)^3 \quad . \tag{2}$$

The $\Delta\sigma$ values fall within a wide range from 0.113 to 12.190 MPa (listed in Table 1). Our estimates for this sequence are generally lower than those observed in central Italy: 0.2–25.0 MPa for the 2009 L'Aquila seismic sequence with M_L = 3.0–5.9 [12], an average of ~2 MPa for the Umbria–Marche seismic sequence with M_L = 1.4–5.9 [7, 8], and approximately 0.3–30.0 MPa for a large number of events of M_L = 3–6 during 2008–2013 in central Italy [20]. The $\Delta\sigma$ values for M_L < 5.0 events, 0.113–2.905 MPa, show an approximate trend of slow increase with increasing M_w, which can be described approximately by a lognormal distribution with a mean of 0.709 MPa and a standard deviation of 0.333 on the base-10 log scale. However, the $\Delta\sigma$

values for $M_L > 5.0$ events, 5.475–12.190 MPa with a mean of 7.149 MPa and a standard deviation of 0.123 on the base-10 log scale, exhibit small variation with M_w. The three largest events (M_L 6.0, 5.9, and 6.1) resulted in high stress drops of 9.775, 5.618, and 12.190 MPa, respectively. The higher $\Delta\sigma$-variability for smaller events ($M_L < 5.0$) could indicate that small earthquakes are likely to propagate in a rough fluctuating stress field, while large earthquakes propagate across a relatively smooth correlated field, as argued by [21] and [22]. During earthquake failure, the slip increases with rupture dimension considerably less in a strongly heterogeneous stress field than it does in a relatively homogenous stress field [23]. Since the stress drop on a given rupture area correlates with the amount of slip, this might explain the increasing stress drops with the event size.

Table 1 – Basic information for events analyzed in this study and estimated source parameters.

Eq No.	**Date**	**Time (UTC)**	‡M_w	‡$\Delta\sigma$ **[MPa]**	**Eq No.**	**Date**	**Time (UTC)**	‡M_w	‡$\Delta\sigma$ **[MPa]**	**Eq No.**	**Date**	**Time (UTC)**	‡M_w	‡$\Delta\sigma$ **[MPa]**
1†	2016/08/24	01:36:32	5.98	9.775	27	2016/10/26	21:24:51	3.80	0.776	53†	2016/11/12	14:43:33	4.18	0.644
2	2016/08/24	01:56:03	4.63	0.651	28†	2016/10/26	21:42:01	4.56	1.676	54†	2016/11/14	01:33:43	3.99	0.922
3	2016/08/24	02:05:57	4.03	0.435	29	2016/10/26	23:52:32	3.69	0.113	55	2016/11/14	19:49:52	3.85	0.606
4	2016/08/24	02:07:30	4.05	0.198	30	2016/10/27	00:21:32	3.68	0.160	56†	2016/11/27	21:41:14	4.02	0.296
5†	2016/08/24	02:33:29	5.21	5.475	31	2016/10/27	01:37:07	3.58	0.465	57†	2016/11/29	16:14:02	4.23	1.251
6	2016/08/24	02:59:35	4.05	0.813	32†	2016/10/27	03:19:27	4.11	0.592	58†	2016/12/01	11:30:53	4.08	0.370
7	2016/08/24	03:08:10	3.77	0.598	33†	2016/10/27	03:50:25	4.41	0.683	59	2016/12/11	12:54:52	4.45	1.036
8	2016/08/24	03:40:11	4.12	1.034	34†	2016/10/27	08:21:47	4.28	1.383	60†	2017/01/18	09:25:42	4.99	6.911
9†	2016/08/24	04:06:50	4.49	0.725	35	2016/10/30	06:40:18	6.13	12.190	61†	2017/01/18	10:14:12	5.24	5.648
10†	2016/08/24	11:50:30	4.60	2.273	36	2016/10/30	07:00:40	3.84	0.410	62	2017/01/18	10:16:39	4.62	0.702
11	2016/08/24	14:02:21	4.13	0.273	37	2016/10/30	07:07:54	4.08	0.493	63	2017/01/18	10:24:16	3.91	1.053
12†	2016/08/24	17:46:09	4.28	2.046	38	2016/10/30	07:13:06	4.14	2.178	64	2017/01/18	10:25:26	5.05	6.139
13	2016/08/24	23:22:05	3.93	0.362	39	2016/10/30	07:34:47	3.97	0.925	65	2017/01/18	10:39:24	4.00	0.902
14†	2016/08/25	03:17:16	4.39	2.745	40	2016/10/30	10:19:26	3.87	1.550	66	2017/01/18	11:07:39	4.16	1.364
15†	2016/08/25	12:36:06	4.39	0.661	41	2016/10/30	11:21:09	4.08	0.535	67†	2017/01/18	13:33:37	4.89	6.414
16†	2016/08/26	04:28:25	4.73	1.173	42†	2016/10/30	11:58:17	4.06	0.577	68	2017/01/18	15:16:13	4.42	0.472
17	2016/08/27	02:50:59	4.18	0.257	43†	2016/10/30	12:07:00	4.38	1.794	69†	2017/01/18	19:32:32	4.13	1.576
18†	2016/08/28	15:55:35	4.31	1.508	44†	2016/10/30	13:34:54	4.28	1.129	70†	2017/02/03	03:47:55	4.27	0.270
19	2016/08/31	18:12:52	3.71	1.610	45	2016/10/30	14:45:29	3.87	0.254	71†	2017/02/03	04:10:05	4.63	0.367
20†	2016/09/03	01:34:12	4.43	0.787	46	2016/10/30	18:21:09	4.38	0.205	72	2017/02/20	03:13:30	4.08	0.610
21†	2016/09/03	10:18:51	4.42	1.670	47†	2016/10/31	03:27:40	4.15	1.710	73	2017/04/09	01:52:28	3.63	0.500
22	2016/09/19	23:34:29	3.97	0.943	48†	2016/10/31	07:05:45	4.09	1.261	74	2017/04/27	21:16:59	4.37	0.183
23	2016/10/16	09:32:35	4.15	0.703	49†	2016/11/01	07:56:39	4.64	2.060	75	2017/04/27	21:19:43	4.23	0.466
24†	2016/10/26	17:10:36	5.18	8.653	50	2016/11/02	19:37:52	4.29	0.141	76	2017/06/24	08:30:09	3.79	0.235
25†	2016/10/26	19:18:06	5.84	5.618	51†	2016/11/03	00:35:01	4.72	2.905	77	2017/06/30	00:25:17	3.92	0.525
26	2016/10/26	19:25:18	3.86	1.132	52†	2016/11/07	18:56:16	3.92	1.151	78	2017/07/22	02:13:07	4.18	1.330

† Events used to discuss the source rupture directivity in this study; ‡ Moment magnitude (M_w), corner frequency (f_c), stress drop ($\Delta\sigma$), and high-frequency decay (κ) computed from the non-parametric GIT in this study.

The magnitude-dependent $\Delta\sigma$ values, shown in Fig. 3(a), indicate a breakdown of earthquake self-similar scaling in this seismic sequence for M_w = 3.58–6.13. The depth-independence (Fig. 3(b)) and scattered spatial distribution within the epicentral area for events with high $\Delta\sigma$ values (Fig. 3(c)) further confirmed the fact that the $\Delta\sigma$ values are dependent on the M_w value (i.e., the breakdown of earthquake self-similar scaling). In central Italy, a breakdown of earthquake self-similar scaling also occurred in the L'Aquila seismic sequence [12, 20], whereas self-similar scaling was followed by the Umbria–Marche seismic sequence over the range of M_L = 1.4–5.9 [7, 8]. The regressed magnitude-dependent $\Delta\sigma$ models based on the L'Aquila events with hypocentral depths of 6–10 km [12] and with hypocentral depths deeper than 8 km [20] are plotted in Fig. 3(a) for comparison with the $\Delta\sigma$–M_w plots of our study. The M_w-independent model for $M_w > 5.0$, proposed by [20], is scaled to the$\Delta\sigma$–M_w plots of our study, although their model reveals larger $\Delta\sigma$ values. Both models also exhibit a trend of increase of $\Delta\sigma$ with M_w when M_w = 4.2–5.0 [20] and when $M_w > 3.9$ [12].

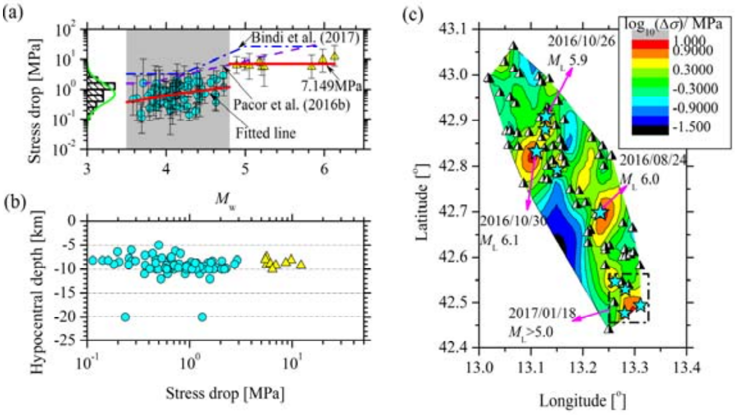

Fig. 3 – (a) Stress drop values vs. moment magnitudes (M_w). The histogram depicts the lognormal distribution of $\Delta\sigma$ values for events of $M_w < 4.80$. Solid lines represent the linear best fit between $\Delta\sigma$ and M_w for $M_w < 4.80$ and $M_w > 4.80$. The $\Delta\sigma$–M_w relationships established by [12] and by [20] are compared. (b) Stress drop values vs. hypocentral depths. (c) Spatial distribution of $\Delta\sigma$ values for events considered in this study.

The 2016–2017 central Italy seismic sequence can be characterized by the occurrence of multiple major earthquakes on the local fault systems within a short period. After the initial mainshock that released high stress drops on the southern portion of the Mt. Vettore–Mt. Bove fault system and on the northern portion of the Laga Mts. fault system (Fig. 1), the small aftershocks that occurred immediately afterwards around the area of the mainshock released low stress drops. However, two months later, the 26 October M_L 5.4 and M_L 5.9 and the 30 October M_L 6.1 events again released high stress drops on the northern portion of the Mt. Vettore–Mt. Bove fault system. The four $M_L > 5.0$ events on 18 January 2017 that occurred to the south of the mainshock produced the final high stress releases in this sequence. The other small aftershocks that occurred intermittently during that time generally showed low stress drops. [24] proposed that earthquakes with high stress drops are likely to induce successive occurrence of multiple major earthquakes resulting from post-seismic stress transfer. Similarly, [25] also verified that high-stress changes from neighboring events cause significant reduction of recurrence intervals. We thus inferred that intensive stress release of the mainshock and relatively lower stress release during subsequent smaller events might cause rapid accumulation of stress on extensional unruptured faults activated in the mainshock, which might be one reason for the occurrence of the subsequent major events. Based on inverted kinematic source models for the three largest earthquakes, [1] suggested the occurrence of subsequent major events and, in part, the rupturing of an already activated fault plane, might have been due to complex effects of the perturbation of stress loads on the volume containing the fault plane.

4. Source rupture directivity

Source rupture directivity is prone to occur not only in most large earthquakes [26] but also in many small–moderate earthquakes [27, 28]. Source rupture directivity effects, strong azimuthal dependence both in the duration of the apparent source time function and in the spectral amplitude of the apparent source spectrum, are usually expressed in the form of $C_d^{0.5}$. Following [29], the rupture directivity coefficient C_d for asymmetrical bilateral rupture propagation under an assumption of a homogeneous kinematic line source model can be expressed as:

$$C_{\mathrm{d}} = \sqrt{\frac{k^2}{\left[1-\left(\frac{v_{\mathrm{r}}}{\beta}\right)\cos\vartheta\right]^2} + \frac{(1-k)^2}{\left[1+\left(\frac{v_{\mathrm{r}}}{\beta}\right)\cos\vartheta\right]^2}}, \qquad (3)$$

where v_r/β is the Mach number, and ϑ is the angle between the ray that leaves the source and the direction of rupture propagation [30], which can be expressed as the difference between the horizontal rupture direction φ and the station azimuth. k represents the relative portion of rupture length in the direction φ accounting for the entire rupture length. In this study, rupture parameters v_r/β, φ, and k were estimated to describe source rupture directivity.

Our study selected 36 of 78 events to investigate their potential source rupture directivity through analysis of the azimuthal dependence in the apparent source spectra. Each selected event was recorded by at least 60 stations of which the site response functions were obtained and that more than 5 stations should be available in each quadrant of a Cartesian coordinate system taking the epicenter as the origin. The apparent source spectra (S_a) at each station were obtained after removing path attenuation and site terms from the S-wave spectra. The residuals, i.e., the differences between the apparent source spectra and the inverted source spectrum on the base-10 logarithmic scale, were calculated at frequencies of 0.25–20 Hz to reflect the azimuthal variation of the apparent source spectra.

Table 2 – Estimated rupture parameters, including φ, v_r/β, and k for the 10 most directive events

Eq No.	**Directivity frequency band[Hz]**	$\varphi^{\dagger}$	$v_r/\beta^{\dagger}$	$k^{\dagger}$	**Eq No.**	**Directivity frequency band[Hz]**	$\varphi^{\dagger}$	$v_r/\beta^{\dagger}$	$k^{\dagger}$
5	0.3–1.0	162.2±3.3	0.85±0.04	0.99±0.01	42	1.5–15.0	176.6±3.4	0.89±0.05	0.99±0.01
9	0.9–2.0	174.4±1.9	0.82±0.02	0.99±0.01	49	7.0–15.0	139.1±1.9	0.81±0.04	0.95±0.03
20	3.0–15.0	332.6±4.8	0.82±0.03	0.94±0.01	56	8.0–15.0	137.2±6.7	0.76±0.02	0.96±0.01
32	2.0–6.0	127.1±10.8	0.80±0.05	0.97±0.01	57	1.5–15.0	296.6±2.0	0.88±0.04	0.98±0.01
34	0.3–8.0	357.5±18.5	0.82±0.05	0.97±0.02	58	1.5–15.0	164.9±4.8	0.85±0.03	0.97±0.01

[†] Mean and the one standard deviation of the rupture parameters retrieved in the directivity frequency band (mean ± one standard deviation); [‡] Computed from the nonparametric GIT in this study.

We applied the $\log_{10}(C_d^{0.5})$ curve to fit the azimuthal residuals at each of the 20 frequencies selected over the range from 0.3–15.0 Hz for each event, according to the least squares method, and we expected to retrieve the optimal rupture parameters, i.e., v_r/β, φ, and k. The values of Max.$C_d^{0.5}$/Min.$C_d^{0.5}$ at the 20 frequencies selected are calculated for each event. We found the majority of events (~26 out of the 36 events considered) show very small Max.$C_d^{0.5}$/Min.$C_d^{0.5}$ values (<2.5) at most frequencies considered, which indicates weak or absent rupture directivity effects. Overall, 10 events (Nos. 5, 9, 20, 32, 34, 42, 49, 56, 57, and 58) have wide frequency bands including at least four continuous frequencies with Max.$C_d^{0.5}$/Min.$C_d^{0.5}$ $\geq$ 2.5, reflecting strong azimuthal variation of the residuals, which is potentially caused by strong rupture directivity. Hereafter, the corresponding frequency band is called the directivity frequency band. Details of the 10 most directive events and their directivity frequency bands with Max.$C_d^{0.5}$/Min.$C_d^{0.5} \geq 2.5$ are listed in Table 2.

An event assumed as a simple line source model can not rupture multiple frequency-dependent planes intersecting at the epicenter but towards different directions, as shown with the gray lines in Fig. 4(a). The strike of the rupture plane can be inferred from the retrieved φ value. Therefore, the reliability of the rupture parameters (i.e., v_r/β, φ, and k) can be evaluated by the stability of the strike of the rupture planes derived at different frequencies. In order to quantify the strike of the rupture plane, the deviation angle in the range from −90° to +90° was proposed, defined as the acute intersection angle between the rupture plane and an alignment passing through the epicenter. If the rupture plane is coincided with the alignment after rotating anticlockwise within 90°, the deviation angle is positive; otherwise, it's negative. We selected one from the two alignments (north–south-trending and east–west-trending alignments) for each event based on the preliminary trial calculation. Fig. 4(a) shows two examples illustrating how to determine the appropriate alignment. The deviation angles at the 20 frequencies for each event, calculated using the selected alignment, are plotted in Fig 4(b). Substantial variability of the deviation angles over all considered frequencies, represented by the error bars, can be observed in 30 events (8 from the 10 most directive events and 22 from the remaining 26 events). However, the remaining six events (Nos. 49, 57, 1, 18, 60, and 67) show small variability of deviation angle (standard deviation < 15°).

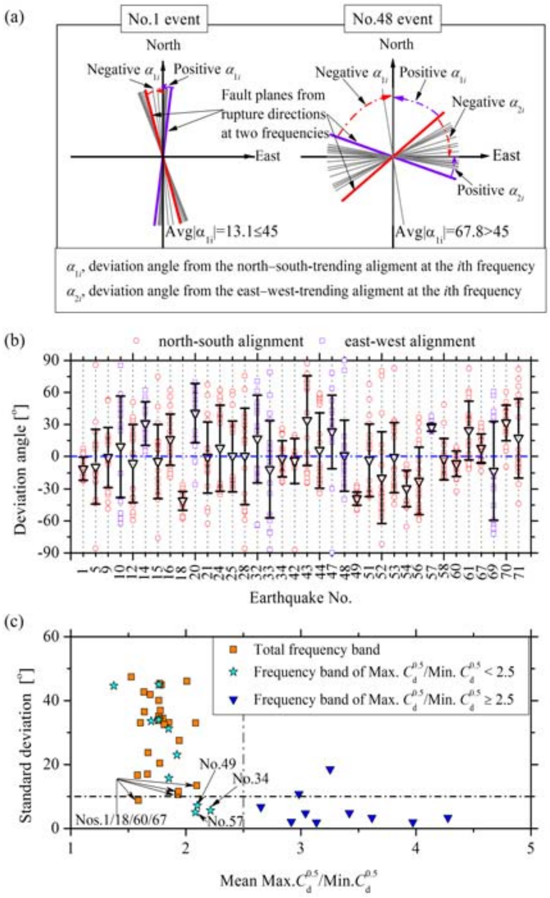

Fig. 4 – (a) Illustrations of how to determine appropriate alignment used to calculate the deviation angles. (b) Deviation angles of the rupture planes from a north–south-trending or east–west-trending alignment at 20 frequencies for each event. (c) Standard deviation of the deviation angles in each group for the 10 most directive events and over the total frequencies for the remaining 26 events against the mean of the

Max.$C_d^{0.5}$/Min.$C_d^{0.5}$ values. For the 10 most directive events, the deviation angles are classified into two groups (stars and triangles) according to the values of Max.$C_d^{0.5}$/Min.$C_d^{0.5}$.

For each of the 10 most directive events, the deviation angles were further divided into two groups according to the corresponding Max.$C_d^{0.5}$/Min.$C_d^{0.5}$ values: one group consisted of deviation angles at the directivity frequency band (in Table 2) and the other group covered those at the remaining frequencies. The standard deviations of the deviation angles in each group for the 10 most directive events and those covering all selected frequencies for the remaining 26 events were calculated and then plotted against the mean of the Max.$C_d^{0.5}$/Min.$C_d^{0.5}$ values over the corresponding frequencies, as shown in Fig. 4(c). For the 10 most directive events, the deviation angles in groups with Max.$C_d^{0.5}$/Min.$C_d^{0.5}$ ≥ 2.5 generally produce small standard deviations (generally $\leq 10°$), indicating the stability of the estimation of the rupture planes hinted by the φ values. The stable estimations preliminarily validate the reliability of the form of $C_d^{0.5}$ for describing the significant rupture directivity effects. Except for three events (Nos. 34, 49, and 57), for which relatively small variability was observed for both groups (Fig. 4(c)), large variability of the deviation angles was found for the group with small Max.$C_d^{0.5}$/Min.$C_d^{0.5}$ values (<2.5) in the other seven events, indicating unstable estimation of the rupture planes for cases of weak or absent rupture directivity effects. Similarly, large variability of the deviation angles covering all selected frequencies was generally observed in most of the remaining 26 events, for which weak or absent rupture directivity was supposed. We thus inferred that the form of $C_d^{0.5}$ is unqualified to express weak or absent rupture directivity effects. However, small variability of the deviation angles was observed in four of the 26 events (Nos. 1, 18, 60, and 67), which might suggest the occurrence of potential rupture directivity. The rupture properties for the four events were also discussed in detail in the later section.

The means and standard deviations for the retrieved rupture parameters (v_r/β, φ, and k) within the directivity frequency bands for the 10 most directive events are provided in Table 2. The φ values confirmed that the ruptures are indeed on the NNW–SSE-striking fault plane, which is close to the NNW–SSE-trending seismogenic fault systems and the major axis of the spatial distribution of the nucleated region of the 2016–2017 seismic sequence (Fig. 1). The k values (mainly > 0.95) consistently reveal approximately unilateral rupture propagation for the 10 most directive events. Some events (Nos. 20, 34, and 57) propagated toward the northwest, whereas other events (Nos. 5, 9, 32, 42, 49, 56, and 58) propagated toward the southeast. The rupture directivity for three events (Nos. 5, 49, and 57) discussed in our study were also investigated by [5]. They also identified unilateral rupture propagation toward the southeast for Nos. 5 and 49 events and toward the northwest for the No. 57 event. The retrieved v_r/β values are mainly within the range 0.80–0.90, indicating fast rupture velocity for the 10 events. Given $c = 3.15$ km/s at the depth of 7.5–14.5 km, following the central Italy Apennines velocity model [17], the rupture velocity is approximately in the range 2.52–2.84 km/s. The approximately unilateral rupture propagation and the reasonably fast rupture velocity reveal strong rupture directivity effects in the 10 most directive events.

For the No. 1 event, the symmetrical bilateral rupture propagation ($k = 0.54\pm0.04$) on the NNW–SSE-trending fault plane ($\varphi = 340.7\pm2.6$) with v_r/β of ~0.71 at low frequencies (0.3–1.0 Hz), but the asymmetrical bilateral rupture with ~90% of the rupture propagating ($k = 0.92\pm0.03$) in the north direction ($\varphi = 357.1\pm8.7$) with v_r/β of ~0.67 at high frequencies (3.0–15.0 Hz), were obtained according to the retrieved rupture parameters in our study. Different results for this event have been determined by some previous studies using data with different frequency bands. The kinematic rupture histories separately inverted by [3] and by [2] using low-frequency waveforms of strong-motion recordings, or jointly inverted by [4] by incorporating data sets of low-frequency strong-motion waveforms, teleseismic waveforms, and GPS data, exhibited the bilateral rupture propagation in the NNW and SSE directions. However, asymmetrical bilateral rupture propagation with clear NNW-trending predominance (~70%) was confirmed by [5] who investigated high-frequency S-wave amplitude variations versus azimuths. It implies that the results of identification of rupture directivity are reliant on the frequency-dependent measurement data used. The rupture velocity of the No. 1 event, i.e., ~2.45 km/s (given $c = 3.15$ km/s at the depth of 8 km [17]), was found close to the value of 2.52 km/s (given $c = 3.15$ km/s) provided by [6] but much slower than the value of ~3.0 km/s reported by [2] and by [3]. The rupture of the No. 18 event was identified as bilateral rupture propagation ($k = 0.57\pm0.08$), and slight predominance of rupture propagation in the ~SE direction (N138.8°) was found. However, events Nos. 60 and 67 were evidently asymmetrical bilateral ruptures with ~90% of the rupture propagation (k = 0.88±0.04, and 0.89±0.02, respectively) in NNW direction (~N350.0°) for the No. 60 event and in the NNE direction (~N8.0°) for the No. 67 event. [5] also identified both events (Nos. 60 and 67) as unilateral ruptures in the NNW direction. The slow rupture velocities for the three events (Nos. 18, 60, and 67) were confirmed by v_r/β of ~0.65.

The directions of horizontal rupture propagation for the 10 most directive events in Table 2 and the additional four events (Nos. 1, 18, 60, and 67) are shown in Fig. 5. Results at high frequency for the No.1 event only are shown. SSE or SEE rupture directivity is a common feature for most events located in the northern area of the No. 1 event; however, the opposite rupture directivity (NNW or NNE) dominates those events located in the southern area.

5. Conclusions

The two-step nonparametric GIT was applied to separate the source spectra for 78 events of M_L = 3.5–6.1 during the 2016–2017 central Italy seismic sequence using the S-wave Fourier spectra of 5135 strong-motion data. Inverted source spectra were used to calculate the source parameters, including the M_0, f_c, and $\Delta\sigma$, according to the ω-square source model. The $\Delta\sigma$ values were found mainly in the range 0.113 to 12.190 MPa. The $\Delta\sigma$ values for events of M_w = 3.58–4.73, in the range 0.113 to 2.905 Mpa, showed a slight trend of increase with increasing M_w. However, the $\Delta\sigma$ values for events of M_w = 4.89–6.13 were in the range 5.475 to 12.190 MPa. The $\Delta\sigma$ values revealed obvious dependence on M_w over the range 3.58–6.13, indicating the breakdown of earthquake self-similar scaling in this seismic sequence.

We selected 36 events to investigate source rupture directivity according to the azimuthal dependence in the apparent source spectra. The large values at directivity frequency bands with Max.$C_d^{0.5}$/Min.$C_d^{0.5} \geq 2.5$ in only 10 events revealed the strong azimuthal variation of the apparent source spectra. The remaining 26 events show very small Max.$C_d^{0.5}$/Min.$C_d^{0.5}$ values at most frequencies considered, indicating the weak or absent rupture directivity effects. The form of $C_d^{0.5}$ is qualified to describe the strong rupture directivity effects, rather than the weak or absent directivity effects, inferred from the stability of the rupture planes hinted by the φ estimations. The rupture parameters obtained for the 10 most directive events at the directivity frequency bands all confirmed the approximately unilateral rupture propagation on the NNW–SSE-striking fault plane with a reasonably fast rupture velocity, i.e., ~2.52–2.84 km/s. Stable φ estimations were also observed in the additional four events (Nos. 1, 18, 60, and 67), although small Max.$C_d^{0.5}$/Min.$C_d^{0.5}$ values were found. The No. 1 event showed symmetrical bilateral rupture at low frequencies (0.3–1.0 Hz) and asymmetrical bilateral rupture with ~90% in the north direction at high frequencies (1.0–15.0 Hz). The No. 18 event had approximately symmetrical bilateral rupture propagation on the approximately NW–SE-striking fault plane, whereas events Nos. 60 and 67 were identified as asymmetrical bilateral rupture propagations with ~90% rupture propagation in the NNW and NNE directions, respectively. The four events all showed reasonably slow rupture velocities (~2.05 km/s). According to the rupture parameters of the 14 events (10 most directive events and an additional four events), we note that SSE or SEE rupture directivity was a common feature for events located to the north of the 24 August mainshock (No. 1), whereas the opposite rupture directivity (NNW or NNE) dominated events to the south.

6. Acknowledgements

Basic information for earthquakes, including epicentral location, hypocentral depth, local magnitude, was obtained from INGV Centro Nazionale Terremoti (http://cnt.rm.ingv.it/). The strong-motion data were derived from the Engineering Strong-Motion database (ESM) accessible at the website of http://esm.mi.ingv.it/. This work was supported by the National Key R&D Program of China (No. 2017YFC1500802), National Natural Science Foundation of China (Nos. 51808514 and 51778589), Natural Science Foundation of Heilongjiang Province (No. E2017065).

7. References

[1] Chiaraluce L, Stefano RD, Tinti E, Scognamiglio L, Micjele M, Casarotti E (2017): The 2016 central Italy seismic sequence: A first look at the mainshocks, aftershocks, and source models. *Seismological Research Lett*ers, **88**(3), 1–15.

[2] Pizzi A, Domenica AD, Gallovič F, Luzi L, Puglia R (2017): Fault segmentation as constraint to the occurrence of the main shocks of the 2016 Central Italy seismic sequence. *Tectonics*, **36**.

[3] Tinti E, Scognamiglio L, Michelini A, Cocco M (2016): Slip heterogeneity and directivity of the M_L 6.0, 2016, Amatrice earthquake estimated with rapid finite-fault inversion. *Geophysical Research Lett*ers, **43**, 10745–10752.

[4] Liu C, Zheng Y, Xie Z, Xiong X (2017): Rupture features of the 2016 M_w 6.2 Norcia earthquake and its possible relationship with strong seismic hazards. *Geophysical Research Lett*ers, **44**, 1320–1328.

[5] Calderoni G, Rovelli A, Giovambattista RD (2017): Rupture directivity of the strongest 2016-2017 central Italy earthquakes. *Journal of Geophysical Research: Solid Earth*, **122**(B1).

[6] Convertito V, Matteis RD, Pino NA (2017): Evidence for static and dynamic triggering of seismicity following the 24 August 2016, M_w=6.0, Amatrice (central Italy) earthquake, *Pure and Applied Geophysics*, **174**(10), 3663–3672.

[7] Bindi D, Spallarossa D, Augliera P, Cattaneo M (2001): Source parameters estimated from the aftershocks of the 1997 Umbria–Marche (Italy) seismic sequence. *Bulletin of the Seismological Society of America*, **91**(3), 448–455.

[8] Bindi D, Castro RR, Franceschina G, Luzi L, Pacor F (2004): The 1997-1998 Umbria–Marche sequence (central Italy): Source, path, and site effects estimated from strong motion data recorded in the epicentral area. *Journal of Geophysical Research*, **109**, B04312.

[9] Bindi D, Pacor F, Luzi L, Massa M, Ameri G (2009): The Mw6.3, 2009 L'Aquila earthquake: Source, path, and site effects from spectral analysis of strong motion data. *Geophysical Journal International*, **179**, 1573–1579.

[10] Calderoni G, Rovelli A, Ben-Zion Y, Giovambattista RD (2015): Along-strike rupture directivity of earthquakes of the 2009 L'Aquila, central Italy, seismic sequence. *Geophysical Journal International*, **203**, 399–415.

[11] Pacor F, Gallovič F, Puglia R, Luzi L, D'Amico M (2016a): Diminishing high-frequency directivity due to a source effect: Empirical evidence from small earthquakes in the Abruzzo region, Italy. *Geophysical Research Lett*ers, **43**, 5000–5008.

[12] Pacor F, Spallarossa D, Oth A, Luzi L, Puglia R, Cantore L (2016b): Spectral models for ground motion prediction in the L'Aquila region (central Italy): Evidence for stress-drop dependence on magnitude and depth. *Geophysical Journal International*, **204**, 697–718.

[13] Abrahamson NA, Silva WJ (1997): Empirical response spectral attenuation relations for shallow crustal earthquakes. *Seismological Research Letters*, **68**(1), 94–127.

[14] Brune JN (1970): Tectonic stress and the spectra of seismic shear waves from earthquakes. *Journal of Geophysical Research*, **75**(26), 4997–5009.

[15] Oth A, Bindi D, Parolai S, Giacomo DD (2011): Spectral analysis of K-NET and KiK-net data in Japan, Part II: on attenuation characteristics, source spectra, and site response of borehole and surface stations. *Bulletin of the Seismological Society of America*, **102**(2), 667–687.

[16] Boore DM, Boatwright J (1984): Average body-wave radiation coefficients. *Bulletin of the Seismological Society of America*, **74**(5), 1615–1621.

[17] Herrmann RB, Malagnini L, Munafò I (2011): Regional moment tensors of the 2009 L'Aquila earthquake sequence. *Bulletin of the Seismological Society of America*, **101**(3), 975–993.

[18] Aki K (1967): Scaling law of seismic spectrum. *Journal of Geophysical Research*, **72**(4), 1217–1231.

[19] Allmann BP, Shearer PM (2009): Global variations of stress drop for moderate to large earthquakes. *Journal of Geophysical Research*, **114**, B01310.

[20] Bindi D, Spallarossa D, Pacor F (2017): Between-event and between-station variability observed in the Fourier and response spectra domains: Comparison with seismological models. *Geophysical Journal International*, **210**, 1092–1104.

[21] Ben-Zion Y, Zhu L (2002): Potency-magnitude scaling relations for southern California earthquakes with $1.0 < M_L < 7.0$. *Geophysical Journal International*, **148**, F1–F5.

[22] Ben-Zion Y, Eneva M, Liu Y (2003): Large earthquake cycles and intermittent criticality on heterogeneous faults due to evolving stress and seismicity. *Journal of Geophysical Research*, **108**(B6), 2307–2327.

[23] Ben-Zion Y (2008): Collective behavior of earthquakes and faults: continuum-discrete transitions, progressive evolutionary changes, and different dynamic regimes. *Reviews of Geophysics*, **46**, RG4006.

[24] Kenner SJ, Simons M (2013): Temporal clustering of major earthquakes along individual faults due to post-seismic reloading. *Geophysical Journal International*, *160*, 179–194.

[25] Chen KH, Bürgmann R, Nadeau RM (2013): Do earthquakes talk to each other? Triggering and interaction of repeating sequences at Parkfield. *Journal of Geophysical Research: Solid Earth*, **118**, 165–182.

[26] McGuire JJ, Zhao L, Jordan TH (2002): Predominance of unilateral rupture for a global catalog of large earthquakes. *Bulletin of the Seismological Society of America*, **92**(8), 3309–3317.

[27] Kane DL, Shear PM, Goertz-Allmann BP, Vernon FL (2013): Rupture directivity of small earthquakes at Parkfield. *Journal of Geophysical Res*earch, **118**(1), 212–221.

[28] Tan Y, Helmberger D (2010): Rupture directivity characteristics of the 2003 Big Bear sequence. *Bulletin of the Seismological Society of America*, **100**(3), 1089–1106.

[29] Boatwright J (2007): The persistence of directivity in small earthquakes. *Bulletin of the Seismological Society of America*, **97**(6), 1850–1861.

[30] Joyner WB (1991): Directivity for non-uniform ruptures. *Bulletin of the Seismological Society of America*, **81**(4), 1391–1395.